

Perceptually Optimized Super Resolution

Volodymyr Karpenko
volodymyr.karpenko@usi.ch

Taimoor Tariq
taimoor.tariq@usi.ch

Jorge Condor
jorge.condor@usi.ch

Piotr Didyk
piotr.didyk@usi.ch

Università della Svizzera Italiana (USI), Lugano, Switzerland

Abstract

Modern deep-learning based super-resolution techniques process images and videos independently of the underlying content and viewing conditions. However, the sensitivity of the human visual system to image details changes depending on the underlying content characteristics, such as spatial frequency, luminance, color, contrast, or motion. This observation hints that computational resources spent on up-sampling visual content may be wasted whenever a viewer cannot resolve the results. Motivated by this observation, we propose a perceptually inspired and architecture-agnostic approach for controlling the visual quality and efficiency of super-resolution techniques. The core is a perceptual model that dynamically guides super-resolution methods according to the human’s sensitivity to image details. Our technique leverages the limitations of the human visual system to improve the efficiency of super-resolution techniques by focusing computational resources on perceptually important regions; judged on the basis of factors such as adapting luminance, contrast, spatial frequency, motion, and viewing conditions. We demonstrate the application of our proposed model in combination with network branching, and network complexity reduction to improve the computational efficiency of super-resolution methods without visible quality loss. Quantitative and qualitative evaluations, including user studies, demonstrate the effectiveness of our approach in reducing FLOPS by factors of 2x and greater, without sacrificing perceived quality.

1. Introduction

Super-resolution (SR) has quickly become a fundamental tool in imaging and media distribution, given the increasing requirements of delivering higher quality content at lower bandwidths, and as general compression tools to deal with escalating imaging sensor resolutions. In me-

dia production such as virtual reality, augmented reality, and video games, SR is indispensable to cater to the high-resolution, high-framerate requirements of modern displays and low power budgets [2, 15, 30, 32]. With the advent of hardware-specific accelerators for efficiently running DL models [31], most modern approaches, even for real-time needs, involve using convolutional neural networks trained on large priors of natural images, which during run-time take low-resolution images as input and produce higher resolution versions. However, even with ever-increasing computational power at our disposal, the computational burden of high-quality SR methods is still problematic [1]. In fact, state-of-the-art methods on real-time SR using neural networks, such as Bicubic++ [7], directly compete with efficient, classic bicubic interpolation techniques, yielding marginal quantitative improvements while still struggling to compete in runtime. Our key insight is that, given that SR images are to be observed by a human, we can take advantage of the naturally compressive capabilities of the human visual system (HVS) to process differently areas of the input image depending on its characteristics and human sensitivity to those, such as spatial frequency, luminance, color, contrast, or even, in the case of videos, motion. Computational resources are allocated to perceptually meaningful areas, as determined by our low-level visual model; analogously to how lossy compression schemes such as JPEG similarly allocate memory by leveraging the HVS.

This observation is the foundation of our work. First, we model the output attenuation (in the frequency domain) of baseline SR neural networks after each layer. Then, after dividing an image or individual frame into a set of patches, our perceptual model (grounded on recent work on contrast-sensitivity functions [28]) predicts how many layers of the network should the patch be processed through; perceptually sensitive patches will be processed by the whole model, whereas the least perceptually meaningful content will simply resort to bicubic interpolation, Fig. 1 shows a visual ex-

ample. We apply our model to other use cases (with the goal of computational efficiency) such as selecting a network of appropriate depth from a set of candidates. In all of these cases, the goal is make the inference as fast as possible without noticeable quality degradation. Through a series of user studies and quantitative measurements of quality and runtime, we demonstrate that our perceptual model enables faster runtime at no perceivable loss of quality when compared with the baseline models. Our work can be integrated into any learned super-resolution architecture, and due to its eccentricity-aware vision model, can be particularly relevant to VR and AR applications, where computational efforts are further directed primarily towards areas in the foveal vision, the foundation of foveated rendering approaches [32].

2. Related Work

Single-frame super-resolution Super-Resolution (SR) or image-upsampling has traditionally been addressed through interpolation-based techniques. Nearest-Neighbor, Bilinear or Bicubic interpolation techniques are commonly used, featuring increasingly bigger receptive fields and perceived quality, at the cost of performance. However, interpolation-based techniques that solely consider the input image are fundamentally limited in terms of upsampling capacity, as high frequency signals lost in the downsampled or compressed image could never be recovered from the signal itself. Leveraging natural image statistics, either explicitly [44] or implicitly [39] has shown greater potential, as lost frequencies can be composed from the expected distribution already present in natural images. Implicit (Deep-Learning based) methods have recently received the greatest attention, as large datasets of high resolution images [10, 34] and advances in neural-network architectures [12, 14, 19].

Early efforts were based on convolutional neural networks [11, 17, 41]. In practice, they learned sets of convolutional filters adapted to different features, enabling them to better reconstruct missing frequencies in a content-aware manner. These were usually trained end-to-end via down-sampling HR images and upsampling the result to recover the original signal, usually employing pixel-error or perceptual [47] loss functions. A popular extension of these approaches leveraged adversarial training [13] with latent CNNs for higher quality results [40]. More recently, some methods rely on Vision Transformers [4, 12, 22, 24] for their latent architecture. The self-attention mechanism inherent in the architecture enables capturing long-range relationships within the image content, as opposed to the solely local receptive fields of CNN-based approaches. State-of-the-art methods nowadays rely on diffusion [33] rather than adversarial training [21, 43], featuring improved learning stability and quality. Despite their quality however, diffu-

sion methods (either with vision transformer or CNN backbones) are computationally expensive and usually disregarded in applications where performance is primed.

Temporally-consistent Video SR Temporally-consistent video SR has received ample attention in the literature, for both pre-rendered video [20] and real-time content (i.e. videogames) [2, 15, 30]. The main difference between single image SR is the availability of additional frames, as well as extra information from the rendering engine in the case of videogames (i.e. motion vectors, material information). Traditionally, single-image learning-based approaches struggle to provide consistent SR across frames due to the implicit, difficult-to-interpret latent space they leverage, which does not guarantee temporally consistent outputs. To ensure smoothness across frames, most works simply condition the current frame upsampling on previous or subsequent frames through motion vectors or optical flow to ensure smoothness [30].

There is a fundamental difference between the traditional approach to video SR and our proposal that is important to clarify. Traditionally, video SR methods aim to achieve a better spatial reconstruction due to the availability of multiple frames. However, human sensitivity to spatial details decreases with movement, so a human vision centric approach should leverage this and reduce quality as a function of movement magnitude, without noticeable visual degradation. Our proposed model quantifies the loss of visual acuity with motion, and appropriately decreases the spatial quality of SR. Therefore, we can get faster per-frame SR with videos, in a manner adaptive to factors such as the nature of the content and amount of movement.

3. Background

3.1. Low-Level Human Vision

Owing to evolutionary imperatives of efficiency, the human visual system has evolved to be a compressive system. What this essentially means is that we are not able to resolve all the visual information that is coming into our eyes. The first critical aspect is that due to center surround receptive field of the early visual system, we are much more sensitive to variations in contrast rather than absolute luminance [35]. Furthermore, it is well known that human contrast perception is highly dependent on factors such as spatial frequency and luminance. Due to the nature of the collective receptive field our early human vision, we are most sensitive to a narrow band of spatial frequencies, and our sensitivity falls off at lower and higher spatial frequencies. This phenomena is aptly captured by a model of the early visual system called the Contrast Sensitivity Function (CSF) [5]. The CSF is highly dependent on factors such as local adapting luminance, size of the stimulus, eccentricity, and the amount of movement. For example, universal sensory models such

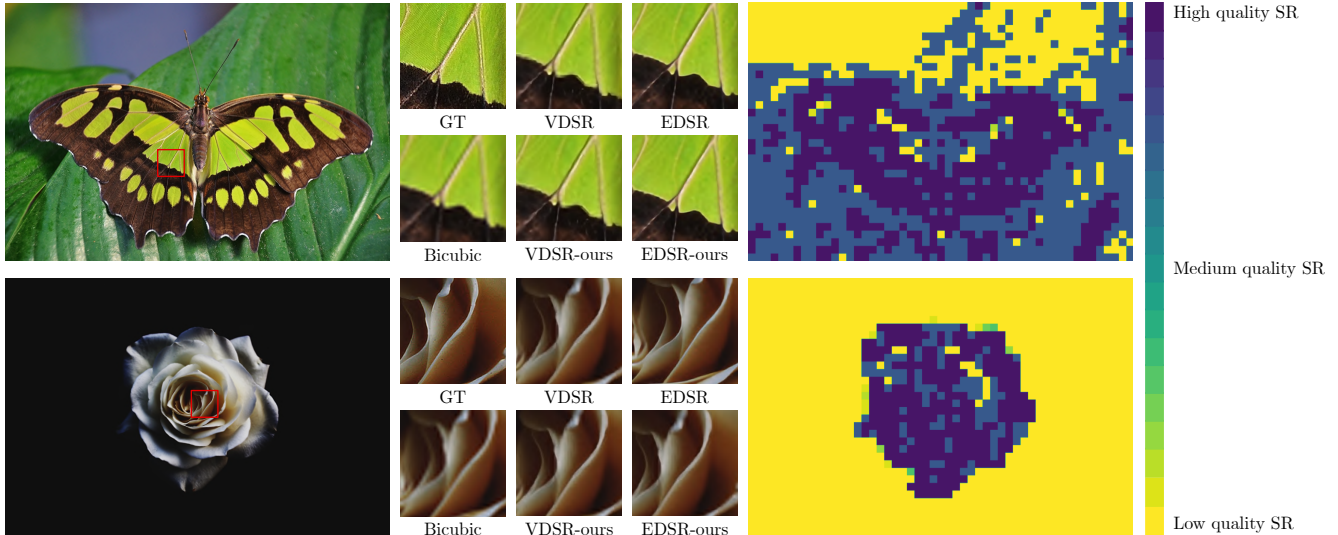


Figure 1. Visual results of our method compared to the original networks on images 829 and 843 from the DIV2K dataset with $\times 4$ super-resolution. On the right, we can observe the maps produced by our perceptual model.

as the Weber-Fechner law tell us that our ability to detect contrast decreases with increasing luminance [26]. Furthermore, due to effects such as contrast masking, neighboring contrast is known to strongly effect human visual perception [37]. This is why we are sometimes less likely to see a loss of resolution in highly textured areas as opposed to independent strong edges. Another very important aspect is that movement or temporal variation decreases our ability to detect and resolve contrast [3]. This behavior is quantified by the dependency of the CSF on temporal frequencies as well as spatial frequencies.

3.2. Visual Difference Predictors (VDP)

Inspired by the compressive nature of human vision, Visual Difference Predictors (VDP) are models that aim to predict the perceived differences between two images based on robustly modeling the frequency selective nature of the early visual system. The framework was originally introduced by Daly et al. [9]. Since then, there have a lot of improvements and extensions to the original model. [26] designed the HDR-VDP, which was one of the first human perception inspired metrics aim to quantify visual differences between HDR images. [27] then extended the VDP to account for human peripheral vision and color [29]. [38] employed the VDP framework to control spatial quality in VR-HMDs. [37] designed a variation of the VDP framework for real-time perceptually optimized tone mapping. Our perceptual model can be thought of as a VDP framework specifically tailored for real-time application to the problem of Deep Learning based Super-Resolution. To the best of our knowledge, our framework is the first application of robust perceptual frameworks to efficient neural network based im-

age/video processing.

4. Method

Our approach is centered around the frequency domain interpretation of super-resolution and the well-established fact that the early visual system is frequency-selective. The main motivation is that the difference between low and high-resolution images lies in the attenuation and removal of higher spatial frequencies. The task of an SR neural network is to reconstruct the missing high spatial frequencies. The better and stronger the neural network, the better the reconstruction. The main idea behind our work is that due to the limitations of the human visual system, we do not always need a perfect reconstruction. If we can quantify the spectral nature of an SR method, we can guide the method using models of visual perception to deliver the least expensive reconstruction required for optimal visual quality, i.e., any further improvement in reconstruction leads to no perceptual benefit while wasting computational resources.

While there are various ways to control the trade-off between the computational efficiency of an SR method and the reconstruction quality, we consider two: network branching and altering network depth. The first approach adds earlier exit points to the original network. Using earlier exit points, i.e., shallower branches, leads to less computation and lower reconstruction quality. In the latter method, different variants of an SR method are created by varying the depth of the original network to make shallower networks more efficient yet potentially comprising the visual quality of the output. Our method is not limited to the above techniques, and others, such as network quantization, could be easily incorporated.

Given different variants of an SR method, our method aims to predict which version should be used in a specific region of an image or video frame. We propose to use attenuation curves to first quantify the reconstruction capability of a given variant. The attenuation curves express the ratio of the radially averaged 2D Fourier transform of the reconstructed output and its full-resolution counterpart. We demonstrated that such curves can be computed on a set of images and reused. Furthermore, we design a perceptual model that expresses the required reconstruction quality in the form of the attenuation curve. Later, our method selects an appropriate SR variant to ensure adequate reconstruction quality for a region while minimizing computational costs. In practice, our method works on image patches which are both input to the SR method and our prediction. Below, we describe all the components of the method followed by the results.

4.1. Attenuation Response Estimation

For a given SR method and an input image, we can quantify the quality of reconstruction by comparing the magnitude of the Fourier Transform of the reconstructed image and its ground-truth version. Given a ground-truth image I , we first downscale it by a factor k , producing image $I_{\downarrow k}$. Later, we use a super resolution method to upscale that image back to its original resolution. Comparing the Fourier transform of the resulting image \hat{I} and the ground-truth counterpart I , allows us to quantify the reconstruction power of the analyzed SR method. More formally, given a super-resolution method ϕ and a test image I , we define the frequency dependent attenuation curve as:

$$\alpha_k^\phi(I, f) = \frac{|\mathcal{F}(\phi(I_{\downarrow k}))(f)|}{|\mathcal{F}(I)(f)|},$$

where \mathcal{F} denotes the Fourier transform. Since we are interested in characterizing the reconstruction capability of the method, we do not compute the curve for one image but for a set of images $\{I_k\}$ and compute for a given SR method ϕ and downscaling factor k the aggregated attenuation response curve as an average across all the images:

$$\alpha_k^\phi(f) = \sum_{i=1}^N \alpha_k^\phi(I_i, f).$$

Although not guaranteed, the value of α_k^ϕ is expected to lie on $(0, 1)$ range, where $\alpha_k^\phi(f) = 0$ means that the SR method was not able to reconstruct content at spatial frequency f , while $\alpha_k^\phi(f) = 1$ indicates the full capability in reconstructing this part of the signal. It has to be noted that this measure quantifies the presence of the signal in the reconstructed output and not its correctness. Nevertheless, we use this as a proxy for the reconstruction quality. This

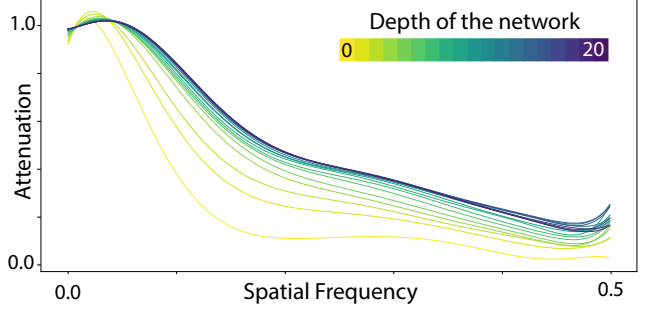


Figure 2. The attenuation curves derived for the case of modulating the depth (number of layers) of the network. Depth equal 0 corresponds to a bicubic upsampling. As the depth of the network is reduced the performance of the solution in reconstructing high-spatial-frequency signal is reduced. The units of the spatial frequency in the plot are cycles-per-pixel.

choice was further motivated by the fact that, although neural networks are non-linear functions, super-resolution is a low-level task with consistent and deterministic characteristics in the frequency domain. The average spectrum of natural images is known to adhere to consistent Fourier characteristics like the inverse power law fall-off. Thus, an average attenuation curve is a good approximation for network response to a general natural image for the task of SR. In order to be more conservative, there is a possibility to use a particular percentile or quartile around the average, but our empirical analysis did not reveal it necessary, which is later confirmed by the results of our user experiments.

For all the variants of the super-resolution techniques considered in this work, we pre-compute the attenuation response curves using the above procedure. We always use 19 natural images from the set5 [6] and set14 [46] datasets, and compute different sets of curves for downscaling parameter $k \in \{2, 4, 8\}$. Fig. 2 presents a set of curves for the case of varying the network depth. After estimating the attenuation curves for variants of SR methods, the next step is to estimate which of them is ideal for a given patch of the image or video frame.

4.2. Perceptual Contrast Modeling

The first step is to convert normalized pixel values into physical luminance units as seen by the visual system. We achieve this by first linearizing the input intensity values, and applying a forward display model [25] as:

$$L_{disp}(p) = (I_{in}(p))^\gamma \cdot (L_{max} - L_{black}) + L_{black} + L_r \quad (1)$$

where $L_{disp}(p)$ is the displayed luminance in nits, $I_{in}(p)$ is the normalized pixel intensity value for the pixel p , γ is the display gamma, L_{max} is the peak brightness of the display, L_{black} is the black level of the display, and L_r is the ambient light reflected from the display surface.

Our visual system is attuned to detect and process contrast, and the efficacy depends on factors such as spatial frequency, content viewing distance, adapting luminance, and amount of motion. Models such as the CSF (which are the base for our VDP framework) usually study the perception of Michelson contrast of Gabor patches with different characteristics [27]. The Michelson contrast of a Gabor patch can be defined as:

$$C_{michelson} = \frac{L_{max} - L_{min}}{L_{max} + L_{min}} \quad (2)$$

In order to get a very fast multi-scale representation of pixel-wise Michelson contrast in the input image, we construct a contrast pyramid [27]. A contrast pyramid level is an element-wise ratio between a Laplacian pyramid ($\Delta L(f, p)$) and Gaussian pyramid level ($L_a(f, p)$). Each level is centered around a band of spatial frequencies, and encodes contrast in the specific range:

$$C(f, p) = \frac{\Delta L(f, p)}{L_a(f, p) + \epsilon} \quad (3)$$

and

$$f = 2^{-(l+0.5)} \cdot ppd \quad (4)$$

where f is the spatial frequency in cycles per visual degree, and p is the pixel index, l is the pyramid level number, and ppd is the pixels per visual degree that the image spans on the human eye (dependent on display dimensions and viewing distance). It is important to point out that the Gaussian pyramid level used is one higher than the Laplacian pyramid, to account for the local luminance adaption region size in human vision (approx 0.5-1 visual degrees) [37]. The contrast pyramid encodes contrast in physical units, the next step is to perceptually normalize it. As we are interested in the detectability of changes in contrast, our problem is more near-threshold than supra-threshold. For near threshold contrast perception modeling, we can normalize physical contrast by multiplication with the corresponding CSF value.

$$C_n(f, p) = C(f, p)S_{CSF}(f, \omega, L_a(f, p)) \quad (5)$$

where ω is the temporal frequency in Hertz. Now, as the CSF is usually measured with Gabor patches on gray backgrounds, it does not account for the visual masking neighboring contrast does to reduce visibility. We model contrast masking as visibility threshold elevation due to the neighboring contrast through a transducer function. The important aspect to remember is that the strongest masking signal is the octave closest to the base contrast, so we only need to consider masking in the same contrast pyramid level as the base contrast [45]. So the final perceptual contrast measure in Just Noticeable Difference (JND) units comes out to be:

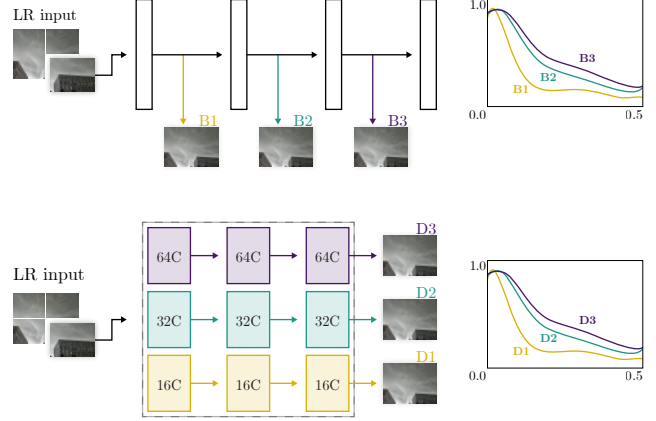


Figure 3. Flowchart illustrating the methodology employed for efficient SR. The input image is divided into patches. For each patch, our task is to estimate which branch B (for the branching case) and which network D (for the depth case) should be used to each patch. The estimation is made through analyzing the computed attenuation characteristics (right). Such as to minimize computations with noticeable quality degradation.

$$C_t(f, p) = \frac{\text{sign}(C_n(f, p)) \cdot |C_n(f, p)|^\alpha}{1 + \frac{1}{|N|} \sum_{q \in N(p)} |C_n(f, q)|^\beta} \quad (6)$$

Here, the numerator models the effect of self-masking, while the denominator models the effect of spatial masking from the 5×5 neighborhood in the same band. If the neighboring pixels/region have contrast on similar spatial frequencies, the effective perceptual contrast is reduced due to masking. $\alpha, \beta \in [0, 1]$ are parameters of our model controlling masking modeling. The value used in our model are $\alpha = 0.7$ and $\beta = 0.2$.

4.3. Perceptual Optimization

Given an input image or an image patch, the goal of the perceptual optimization is to find the maximum attenuation that is tolerable by the HVS. We model the attenuation curve using Gaussian fall-off:

$$\alpha'(f) = \frac{1}{a\sqrt{2\pi}} \exp\left(-\frac{(f-b)^2}{2a^2}\right) + c \quad (7)$$

where f is the spatial frequency and a, b, c are parameters that we wish to estimate. According to the contrast model, the attenuation remains undetectable by an observer if the contrast difference between the original image and the attenuated one is under 1 JND. Consequently, to find the attenuation that results in maximum performance gains yet imperceptible quality loss, we optimize the attenuation curve such that it results in exactly 1 JND difference, i.e.,

$$\forall_f C_t(p, f) - C'_t(p, f) = 1, \quad (8)$$

where $C_t(p, f)$ represents the perceptual contrast of the input image patch and $C'_t(p, f)$ represents the perceptual contrast of the network output. Assuming the the attenuation curves are a response of the network/branch to the input, the attenuation is a modulation of the physical image contrast at different frequencies.

$$\alpha'(f) = \frac{C'(f, p)}{C(f, p)} = \frac{C'_n(f, p)}{C_n(f, p)} \quad (9)$$

where $C_n(f, p)$ is the CSF multiplied input contrast encoded by our contrast pyramid, and our immediate goal is to estimate the tolerable output contrast $C'_n(f, p)$ as constrained by Eq. (7). We aim to estimate values a , b , and c for which the following equality holds:

$$\frac{\text{sign}(C_n(f, p)) \cdot |C_n(f, p)|^\alpha}{1 + \frac{1}{|N|} \sum_{q \in N(p)} |C_n(f, q)|^\beta} = \frac{\text{sign}(C'_n(f, p)) \cdot |C'_n(f, p)|^\alpha}{1 + \frac{1}{|N|} \sum_{q \in N(p)} |C'_n(f, q)|^\beta} \quad (10)$$

It is evident that $C'_n(f, q)$ cannot be directly calculated from this equation due to the visual spatial masking term present in the denominator. Consequently, we make the assumption that the contrast masking for the up-sampled output patch can be approximated by that of the input patch. Furthermore, assuming that the sign of the contrast remains unaltered throughout the neural network processing Eq. (10) can be simplified to:

$$\frac{\text{sign}(C_n(f, p)) \cdot (|C_n(f, p)|^\alpha - |C'_n(f, p)|^\alpha)}{1 + \frac{1}{|N|} \sum_{q \in N(p)} |C_n(f, q)|^\beta} = 1 \quad (11)$$

From this equation, we can derive $C'_n(f, p)$ directly as follows:

$$C'_n(f, p) = \left| |C'_n(f, p)|^\alpha - \left(1 + \sum_{q \in N(p)} \frac{|C'_n(f, q)|^\beta}{|N|} \right) \right|^{1/\alpha} \quad (12)$$

It should be noted that the sign of the contrast is omitted since the focus is on the magnitude of the contrast itself. Now assuming that we have three levels of the contrast pyramid, tolerable attenuation at three different spatial frequencies can be calculated as follows:

$$t_1 = \frac{C'(f_1, p)}{C(f_1, p)}, t_2 = \frac{C'(f_2, p)}{C(f_2, p)}, t_3 = \frac{C'(f_3, p)}{C(f_3, p)} \quad (13)$$

The required values of a , b , and c can be estimated by fitting the attenuation model from Eq. (7) to the three data points: $\alpha'(f_i) = t_i$ for $i \in \{1, 2, 3\}$. Subsequently, the network/branch that will produce the most closely approximating attenuation for the given patch is selected. The selection

of the branch is made in accordance with the following procedure:

$$\text{branch} = \max_{i \in [0, \dots, n]} \left\{ \frac{t \cdot \hat{t}_i}{\|t\| \|\hat{t}_i\|} \right\} \quad (14)$$

where t is the vector of the computed attenuations and \hat{t}_i is the vector of the estimated attenuation produced by Eq. (7).

4.4. Model Efficiency

In our application, it is essential that the overhead of the perceptual model is minimal compared to the performance improvements provided by the SR method. Although we prototyped our solution using Python and evaluated it on a single CPU thread, it has been shown that a similar processing pipeline can be implemented efficiently on a GPU. This is primarily due to the nature of the computation, which consists of independent per-pixel operations (see Eq. 12). Additionally, the construction of the contrast pyramid can be accelerated using MIPMAP functionality. Recently, [37] have demonstrated a perceptual model on the Meta Quest 2 VR headset, achieving 2K resolution with a single execution time of under 1 ms.

5. Experimental Setup

In this section, we go through the methodology to validate the efficacy of our approach.

5.1. Validation SR Models

As mentioned in Section. 4, we employ our perceptual model to optimize SR for two cases. The first approach adds earlier exit points (branches) to the original network. Using earlier points, i.e., shallower branches, leads to less computation and lower reconstruction quality. To test this case, we employ the popular and seminal VDSR [18] network. In the case of VDSR, a neural network with 19 branched outputs was created as per the setting in Fig. 3 (top). After each ReLU activation function, an exit point was added, structured identically to the final layer of the original network., similar to [16]. Our task was to use the perceptual model to select the appropriate branch (per image patch) such that there is no noticeable quality loss.

The second approach is reducing the depth or number of channels of a network to make it more efficient. In this case, we have a number of candidate networks with different number of channels-per-layer, and our task is to employ our perceptual model to select the appropriate one per image patch. To test this case, we employ the EDSR [23] network. In the case of EDSR, five networks with varying numbers of channels per layer (256, 128, 64, 16, 8) were trained independently, the training procedure was the same as described in [23]. Our task was to use the perceptual model to select the appropriate network (per image patch) such that there is no noticeable quality loss.

We selected the two candidate networks because of their popularity and robustness and demonstrated efficacy over the years. Our algorithm is network agnostic as all SR models will follow similar attenuation characteristics, which are grounded in the nature of natural images and the Fourier nature of the SR problem. So to the best of our knowledge, we do not foresee any issues for its application to other SR models.

To evaluate the effectiveness of our method, we tested the model on images and videos, as our model is additionally capable of processing information about the temporal frequencies present in videos.

5.2. Input Patch Size

The input patch size (size of patches into which the image is divided, as shown in Fig. 3) to our perceptual model is equivalent to the size of the receptive field of the upsampling model employed. In the case of the VDSR network, the input patch is $\frac{40}{k} \times \frac{40}{k}$ pixels. This is due to the fact that, during the perceptual model prediction, the low-resolution image is being considered. Before being conveyed to the VDSR network, the LR image is upsampled through bicubic interpolation. Consequently, in the event of $\times 4$ upsampling, the input to the perceptual model is 10×10 pixels, corresponding to a patch of 40×40 pixels in the image upsampled with bicubic interpolation. In the case of the EDSR network, the input patch is 48×48 pixels, taken from the low-resolution image. As no prior upsampling is involved in the input image, there is no need to consider a lower-size patch. In certain instances, utilizing input patches smaller than the neural network’s receptive field may be advantageous, particularly in the context of smaller images.

5.3. Subjective Quality Study

Setup For our experiments, we assumed standard office conditions where the content is viewed on a 27-inch Dell U2723QE display with a resolution of 3840×2160 and a peak luminance of 400 cd/m^2 from the viewing distance of 60 cm. The perceptual model was initialized according to this setup. During our experiments with human subjects, the viewing distance was controlled with the use of a chin rest that allowed to maintain constant viewing conditions throughout the experiments for all participants.

Task We employed a 2AFC experimental protocol. The task was a forced choice between two test cases in relation to a given high quality reference. Users were instructed to select the test case which was perceptually more similar to the reference. On the right half of the screen was always the high quality reference, and the left had either case A or B in randomized order. Users could use the space-bar to switch between A and B, and press ENTER when they had made their choice. The two test cases were

- **A:** the output of our perceptually optimized algorithm

that selects the appropriate network/branch for the corresponding image patch.

- **B:** The output of the unaltered full deep network applied to the whole image.

Stimuli We employed 24 high quality natural scenes for our user study. The scenes were selected for diversity in characteristics such as luminance, contrast and texture.

6. Results and Discussion

6.1. Quantitative Results

The quantitative results for the image datasets are presented in Tab. 1. The proposed method allows for comparable performance to the original networks while reducing the computational cost. For instance, the $\times 2$ and $\times 4$ upsampling operations exhibit a reduced computational cost ranging from 58% to 22% and from 70% to 20%, respectively.

As anticipated, greater savings achieved with $\times 2$ upsampling in comparison to $\times 4$ upsampling is in line with expectations. This is due to the increased presence of high-frequency information in the images, which allows for reconstructing certain parts of the image with less computational power.

In order to evaluate the video, we estimated the optical flow. Subsequently, we calculated the temporal frequency that was necessary for our model, based on the velocities obtained with the optical flow. The frame rate considered for each video was 24 fps. The results for the video datasets are presented in Tab. 2.

6.2. Subjective Quality Results

Metrics such as PSNR, SSIM etc are not representative of the intricacies of how humans perceive image quality. As our perceptual model is based on robust and detailed modeling of early human vision, our hypothesis such that the is little noticeable quality loss can only be aptly verified using subjective quality studies.

Fig. 4 shows the results of our 2AFC user study on images for the network branching application case on the VDSR. It can be seen that on average, the preference value hovers around 50%, which is indicative that users were not able to perceive any difference between the test cases A and B in relation to the reference, which supports our initial goal and hypothesis. The interesting but (but not surprising) observation is that no perceived differences were observed even with the reported differences in PSNR and SSIM reported in Tab. 1. This is because these metrics are completely unaware of human vision, and our model specifically models it. The results for the perceptual study on videos are provided in the supplementary document, which demonstrates the efficacy of our perceptual model for handling motion perception too.

For the channel depth application study, we used the

Table 1. Quantitative comparison on image datasets

| Method | Scale | Set5 | | | Set14 | | | BSD100 | | | Urban100 | | | DIV2K | | |
|-----------|-------|-------|-------|----------------------|-------|-------|----------------------|--------|-------|----------------------|----------|-------|----------------------|-------|-------|--------------------|
| | | PSNR↑ | SSIM↑ | FLOPS↓ | PSNR↑ | SSIM↑ | FLOPS↓ | PSNR↑ | SSIM↑ | FLOPS↓ | PSNR↑ | SSIM↑ | FLOPS↓ | PSNR↑ | SSIM↑ | FLOPS↓ |
| Bicubic | ×2 | 32.32 | 0.923 | | 28.60 | 0.859 | | 28.22 | 0.834 | | 25.48 | 0.840 | | 31.23 | 0.898 | |
| VDSR | ×2 | 34.15 | 0.946 | 89.60G (100%) | 29.98 | 0.899 | 173.68G (100%) | 29.68 | 0.885 | 131.04G (100%) | 27.17 | 0.900 | 144.99G (100%) | 32.65 | 0.931 | 2.04T (100%) |
| VDSR-ours | ×2 | 32.53 | 0.936 | 51.99G (58%) | 29.29 | 0.895 | 100.18G (57%) | 29.40 | 0.883 | 61.63G (47%) | 26.48 | 0.889 | 85.43G (58%) | 32.08 | 0.928 | 1.06T (51%) |
| EDSR | ×2 | 36.42 | 0.954 | 1.54T (100%) | 32.03 | 0.905 | 2.97T (100%) | 30.62 | 0.888 | 2.25T (100%) | 30.42 | 0.932 | 2.56T (100%) | 34.84 | 0.939 | 31.64T (100%) |
| EDSR-ours | ×2 | 36.00 | 0.951 | 353.09G (22%) | 31.58 | 0.901 | 691.09G (23%) | 30.26 | 0.882 | 466.39G (20%) | 29.74 | 0.925 | 606.62G (23%) | 34.25 | 0.925 | 7.27T (22%) |
| Bicubic | ×4 | 26.98 | 0.790 | | 24.28 | 0.676 | | 24.54 | 0.638 | | 21.89 | 0.642 | | 26.80 | 0.756 | |
| VDSR | ×4 | 28.13 | 0.827 | 89.60G (100%) | 25.01 | 0.709 | 173.68G (100%) | 25.11 | 0.670 | 131.04G (100%) | 22.75 | 0.698 | 572.38G (100%) | 27.52 | 0.786 | 2.04T (100%) |
| VDSR-ours | ×4 | 27.77 | 0.823 | 64.13G (71%) | 24.86 | 0.713 | 118.64G (68%) | 25.08 | 0.670 | 69.27G (52%) | 22.65 | 0.699 | 387.01G (67%) | 27.44 | 0.788 | 1.29T (63%) |
| EDSR | ×4 | 30.60 | 0.878 | 579.49G (100%) | 26.95 | 0.753 | 1.00T (100%) | 26.01 | 0.706 | 695.39G (100%) | 24.82 | 0.776 | 3.16T (100%) | 29.05 | 0.822 | 10.32T (100%) |
| EDSR-ours | ×4 | 30.27 | 0.874 | 145.34G (25%) | 26.69 | 0.750 | 236.71G (23%) | 25.82 | 0.701 | 173.54G (24%) | 24.48 | 0.765 | 746.13G (23%) | 28.75 | 0.816 | 2.46T (23%) |

Table 2. Quantitative comparison on video datasets X4 upscaling

| Method | REDS | | | Vid4 | | | UDM10 | | |
|----------------------------------|-------|-------|-----------------------|-------|-------|-----------------------|-------|-------|-----------------------|
| | PSNR↑ | SSIM↑ | FLOPS↓ | PSNR↑ | SSIM↑ | FLOPS↓ | PSNR↑ | SSIM↑ | FLOPS↓ |
| Bicubic | 26.39 | 0.724 | | 22.44 | 0.614 | | 30.76 | 0.884 | |
| VDSR | 27.11 | 0.756 | 702.24G (100%) | 23.14 | 0.670 | 291.96G (100%) | 31.71 | 0.899 | 680.96G (100%) |
| VDSR-ours w/o temporal frequency | 27.03 | 0.755 | 443.84G (63%) | 23.06 | 0.667 | 194.23G (66%) | 31.62 | 0.903 | 433.30G (63%) |
| VDSR-ours | 26.66 | 0.739 | 173.77G (24%) | 23.05 | 0.667 | 193.00G (66%) | 31.58 | 0.902 | 386.77G (56%) |
| EDSR | 28.27 | 0.791 | 3.24T (100%) | 23.92 | 0.711 | 1.59T (100%) | 34.28 | 0.929 | 3.24T (100%) |
| EDSR-ours w/o temporal frequency | 27.03 | 0.755 | 813.12G (25%) | 23.73 | 0.703 | 348.84G (21%) | 33.78 | 0.924 | 813.96G (25%) |
| EDSR-ours | 27.03 | 0.755 | 586.58G (18%) | 23.73 | 0.703 | 348.84G (21%) | 33.84 | 0.925 | 801.61G (24%) |

same scenes as described in Sec. 5.3. We up-scaled the images using a set of EDSR networks. We trained 5 different networks, with either (256, 128, 64, 16, 8) channels per-layer. The baseline was an EDSR with 256 channels per layer applied uniformly across the whole image. The baseline was compared with SR controlled using our perceptual model, which selected one of the 5 candidate networks per each patch. Fig. 5 shows the results of our 2AFC user study, it can be seen that on average, the preference value hovers around 50%, which is indicative that users wone average not able to perceive any difference between the test cases A and B in relation to the reference. The indicates that our perceptual model controlled the results such that any quality loss is not visible, while using 76.4% less FLOPS.

We also ran a perceptual study on natural videos for the network branching application. The stimuli were derived from seven natural videos from the Inter4k [36] dataset. Each video frame was down-sampled by a factor of eight and then up-sampled by a factor of four using the VDSR network, specifically the network branching application. Fig. 6 shows the findings of our 2AFC user study. It can be observed that the mean preference is around 50%, which suggests that users were unable to perceive a difference between test cases A and B in relation to the reference, even when our method uses 51.3% less FLOPS.

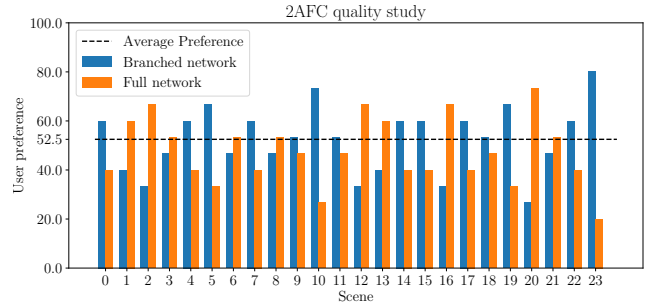


Figure 4. The result of our subjective study (for 15 participants) for the network branching application.

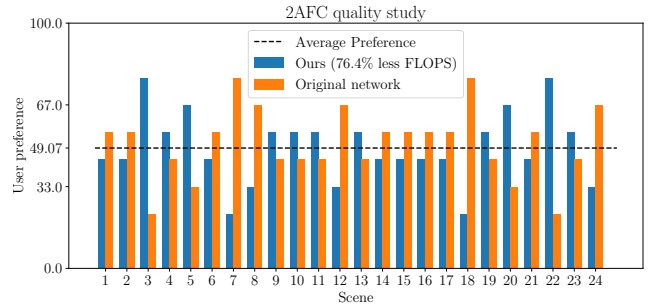


Figure 5. The result of our subjective study (for 9 participants) for the network channel depth application.

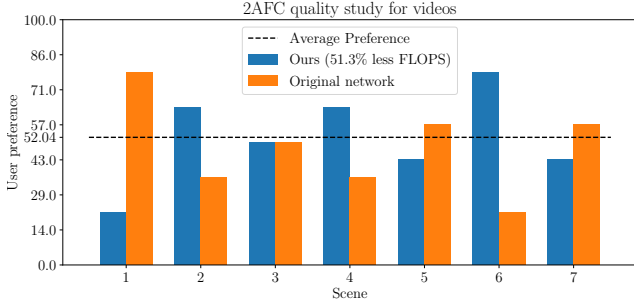


Figure 6. The result of our subjective study (for 14 participants) for the network branching application for videos.

7. Extension - AR/VR Display

Next generation standalone virtual/augmented reality headsets demand high spatial quality, refresh-rate and power efficiency in real-time. Our framework can be applied for gaze-contingent super-resolution for AR/VR headsets. The main justification is that for wide field-of-view displays, human visual acuity decreases significantly away from the gaze-location (fovea). This inhomogeneity is frequently associated with the distribution of retinal cells across the visual field, as demonstrated by [8, 42].

Contrast sensitivity models such as the StelaCSF appropriately model human contrast perception as a function of eccentricity, and thus can extend our model to account for acuity across the visual field. Modern VR/AR headsets have built in eye-trackers that can be used to control our framework. In Fig. 9, we present some preliminary results for our quality map estimation with different gaze positions on the screen. The top row shows the eccentricity map relative to the gaze location, and the bottom row shows how our prediction for required SR quality varies. As anticipated, our perceptual model predicts that higher quality resolution will be used when the user is looking, while for areas in the periphery, our model predicts that the lowest up-sampling quality will be used. The main application is rendering in a lower resolution throughout the field of view, and then up-sampling the rendering for real-time VR/AR displays using our technique. This would especially be beneficial for high quality real-time streaming on AR/VR displays, where the gaze position is not known during transmission and traditional foveated rendering systems would fail, and transmitting a uniformly lower resolution stream and subsequent gaze-contingent up-sampling would be ideal.

8. Future work

Although the method demonstrated expected performance with regard to video content, it was observed that aliasing issues were present. This phenomenon is frequently observed when a single frame is considered in isolation. It

would be of interest to investigate the potential of our perceptual method in conjunction with SR techniques that have been developed explicitly for use in video applications.

The method can be extended to handle color perception by employing the VDP modeling such as ColorVDP [29]. This could enable applications to problems such as deep learning for color constancy/automatic-white-balancing.

Though we applied our perceptual model to control CNN based SR, a similar strategy can be employed for CNN based denoising, frame-interpolation and other low level image/video enhancement tasks. Some modifications to the perceptual modeling may need to be done in a task specific manner. For example, some assumptions about the spectral nature of the noise in denoising, or some pre-processing.

The most interesting open question and future direction is the perceptual control of modern generative models to make them efficient without noticeable loss in visual quality. It is likely that reducing computational complexity in techniques such as latent diffusion would result in similar fourier characteristics of the output i.e a more efficient pipeline (e.g quantized, depth reduction, less channels etc) would result in loss of higher frequencies and our model and pipeline can be applied by studying the attenuation curves similarly. The unclear part is that it might also lead to some structural degradation i.e shape distortion, which may require some additional perceptual modeling as most perceptual models like the VDP rely on pixel wise comparisons. It would be an exciting problem of how the model can be extended to cater for the human perception of such degradations.

9. Conclusions

Contemporary work on image enhancement evaluates the quality of the results in terms of metrics such as PSNR, SSIM, LPIPS etc. Even efforts to make super-resolution techniques efficient are evaluated on these benchmarks, completely ignoring the fact that the final observers are human beings who have an extremely compressive visual system, and the practical goal is to deliver high quality to human observers. We design a robust and very fast perceptual framework that controls the quality of super-resolution in regards to the limitations of human vision, such that computational resources are greatly reduced without any noticeable degradation in visual quality. Our results demonstrate that even with FLOP reductions by factors of-and-greater than 3x, our perceptual algorithm minimally controls the super-resolution output such that the final result is not visually distinguishable from the output of a fully resourced deep network. We optimistically believe that our pipeline can serve as a promising direction for realizing real-time perceptually optimized and controlled image/video enhancement and generative synthesis.

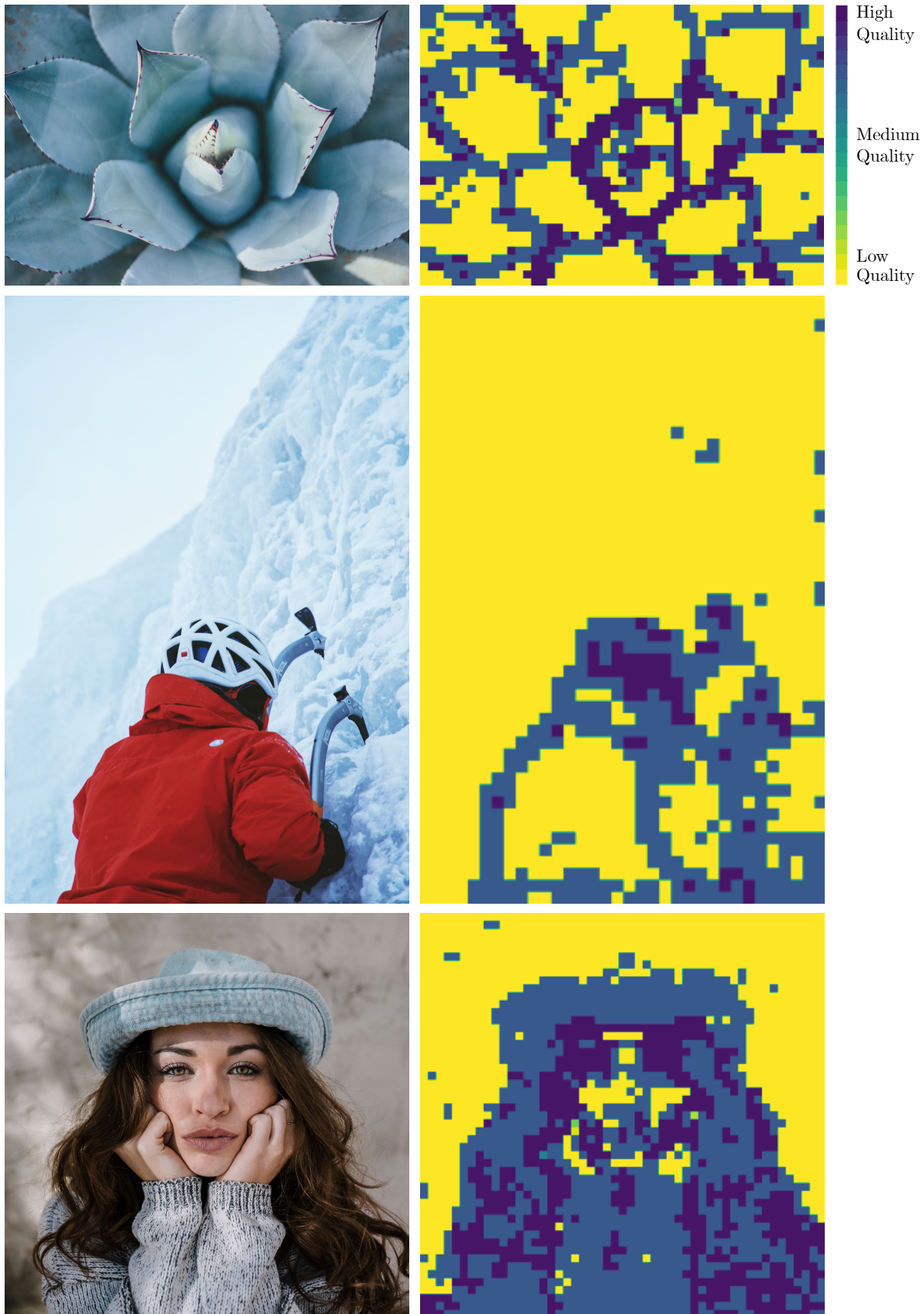


Figure 7. Our method quality map prediction results for $\times 4$ upsampling.

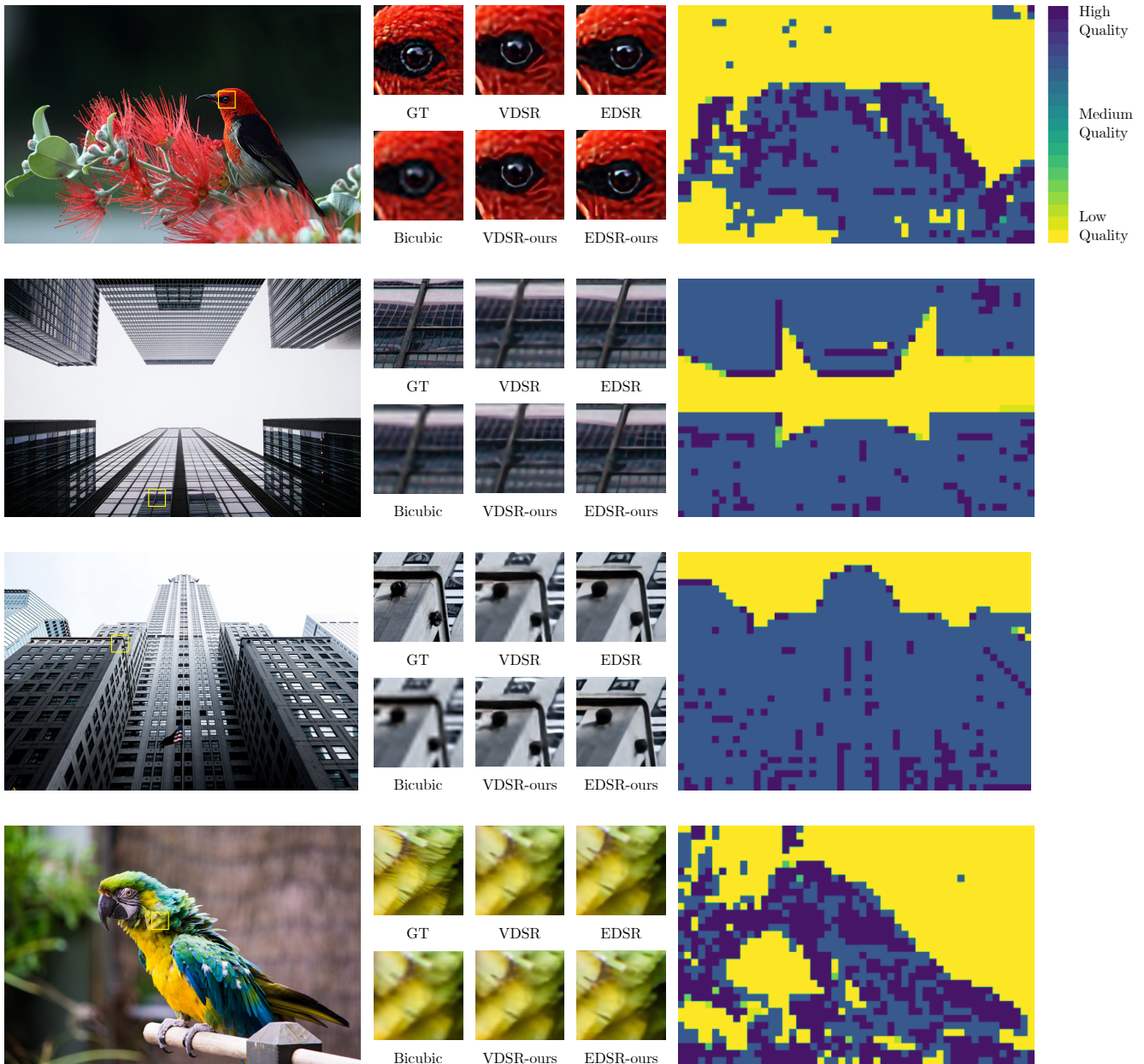


Figure 8. Visual results of our method compared to the original networks. On the right, we can observe the maps produced by our perceptual model.

References

- [1] Adobe Inc. Lightroom super resolution. <https://www.adobe.com/products/photoshop-lightroom/super-resolution.html>, 2024. Accessed: 2024-11-15. 1
- [2] AMD Corporation. Fidelityfx super resolution (fsr). <https://www.amd.com/en/technologies/radeon-software-fidelityfx-super-resolution>, 2024. Accessed: 2024-11-15. 1, 2
- [3] Maliha Ashraf, Rafal K. Mantiuk, Alexandre Chapiro, and Sophie Wuerger. castlesf — a contrast sensitivity function of color, area, spatiotemporal frequency, luminance and eccentricity. *Journal of Vision*, 24, 2024. 3
- [4] Neeraj Baghel, Shiv Ram Dubey, and Satish Kumar Singh. Srtransgan: Image super-resolution using transformer based generative adversarial network. *ArXiv*, abs/2312.01999, 2023. 2
- [5] Peter G. J. Barten. Formula for the contrast sensitivity of the human eye. In *IS&T/SPIE Electronic Imaging*, 2003. 2
- [6] Marco Bevilacqua, Aline Roumy, Christine M. Guillemot, and Marie-Line Alberi-Morel. Low-complexity single-

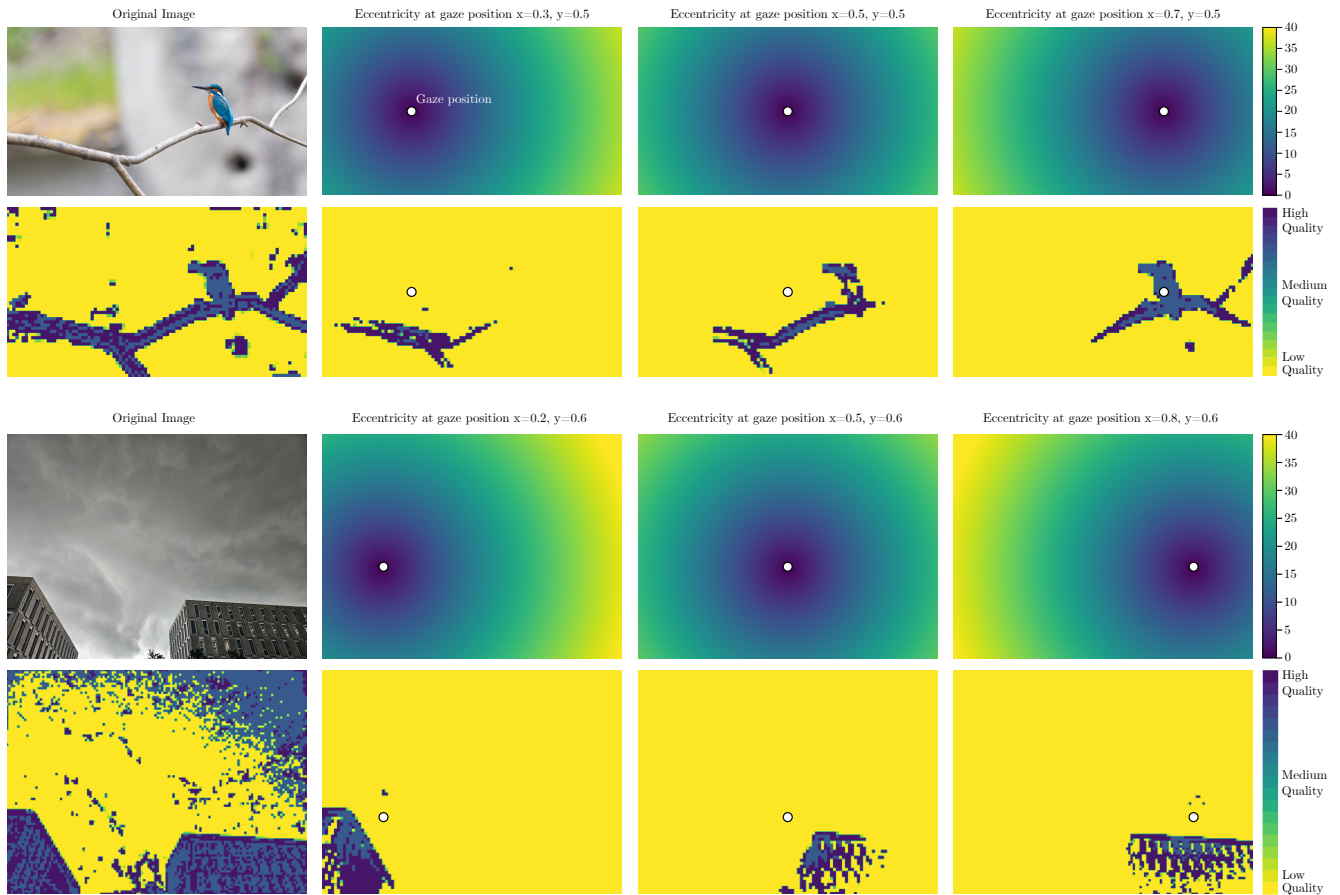


Figure 9. Our model predictions based on gaze position with $\times 4$ super-resolution. In the first column, we have the original image and the corresponding quality map. In the other columns we have on top the eccentricity map expressed in degrees and bottom we have the corresponding quality map.

image super-resolution based on nonnegative neighbor embedding. In *British Machine Vision Conference*, 2012. 4

[7] Bahri Batuhan Bilecen and Mustafa Ayazoglu. Bicubic++: Slim, slimmer, slimmest-designing an industry-grade super-resolution network. In *Proceedings of the IEEE/CVF Conference on Computer Vision and Pattern Recognition*, pages 1623–1632, 2023. 1

[8] C A Curcio and K A Allen. Topography of ganglion cells in human retina. *J Comp Neurol*, 300(1):5–25, 1990. 9

[9] Scott J. Daly. Visible differences predictor: an algorithm for the assessment of image fidelity. In *Electronic imaging*, 1992. 3

[10] Jia Deng, Wei Dong, Richard Socher, Li-Jia Li, Kai Li, and Li Fei-Fei. Imagenet: A large-scale hierarchical image database. In *2009 IEEE Conference on Computer Vision and Pattern Recognition*, pages 248–255, 2009. 2

[11] Chao Dong, Chen Change Loy, Kaiming He, and Xiaoou Tang. Image super-resolution using deep convolutional networks. *IEEE Transactions on Pattern Analysis and Machine Intelligence*, 38:295–307, 2014. 2

[12] Alexey Dosovitskiy, Lucas Beyer, Alexander Kolesnikov, Dirk Weissenborn, Xiaohua Zhai, Thomas Unterthiner, Mostafa Dehghani, Matthias Minderer, Georg Heigold, Sylvain Gelly, Jakob Uszkoreit, and Neil Houlsby. An image is worth 16x16 words: Transformers for image recognition at scale. *ArXiv*, abs/2010.11929, 2020. 2

[13] Ian Goodfellow, Jean Pouget-Abadie, Mehdi Mirza, Bing Xu, David Warde-Farley, Sherjil Ozair, Aaron Courville, and Yoshua Bengio. Generative adversarial networks. *Commun. ACM*, 63(11):139–144, 2020. 2

[14] Kaiming He, X. Zhang, Shaoqing Ren, and Jian Sun. Deep residual learning for image recognition. *2016 IEEE Conference on Computer Vision and Pattern Recognition (CVPR)*, pages 770–778, 2015. 2

[15] Intel Corporation. Xe super sampling (xess). <https://www.intel.com/content/www/us/en/products/docs/discrete-gpus/arc/technology/xess.html>, 2024. Accessed: 2024-11-15. 1, 2

[16] Dohyun Kim, Joongheon Kim, Junseok Kwon, and Tae-Hyung Kim. Depth-controllable very deep super-resolution network. In *2019 International Joint Conference on Neural Networks (IJCNN)*, pages 1–8, 2019. 6

[17] Jiwon Kim, Jung Lee, and Kyoung Mu Lee. Accurate

- image super-resolution using very deep convolutional networks. 2015. 2
- [18] Jiwon Kim, Jung Kwon Lee, and Kyoung Mu Lee. Accurate image super-resolution using very deep convolutional networks. *IEEE Conference on Computer Vision and Pattern Recognition (CVPR)*, pages 1646–1654, 2016. 6
- [19] Alex Krizhevsky, Ilya Sutskever, and Geoffrey E. Hinton. Imagenet classification with deep convolutional neural networks. In *Proceedings of the 25th International Conference on Neural Information Processing Systems - Volume 1*, page 1097–1105, Red Hook, NY, USA, 2012. Curran Associates Inc. 2
- [20] Gen Li, Jie Ji, Minghai Qin, Wei Niu, Bin Ren, Fatemeh Afghah, Lin Guo, and Xiaolong Ma. Towards high-quality and efficient video super-resolution via spatial-temporal data overfitting. *2023 IEEE/CVF Conference on Computer Vision and Pattern Recognition (CVPR)*, pages 10259–10269, 2023. 2
- [21] Haoying Li, Yifan Yang, Meng Chang, Huajun Feng, Zhi hai Xu, Qi Li, and Yue ting Chen. Srdiff: Single image super-resolution with diffusion probabilistic models. *Neurocomputing*, 479:47–59, 2021. 2
- [22] Jingyun Liang, Jie Cao, Guolei Sun, K. Zhang, Luc Van Gool, and Radu Timofte. Swinir: Image restoration using swin transformer. *2021 IEEE/CVF International Conference on Computer Vision Workshops (ICCVW)*, pages 1833–1844, 2021. 2
- [23] Bee Lim, Sanghyun Son, Heewon Kim, Seungjun Nah, and Kyoung Mu Lee. Enhanced deep residual networks for single image super-resolution, 2017. 6
- [24] Zhisheng Lu, Juncheng Li, Hong Liu, Chao Huang, Linlin Zhang, and Tiejong Zeng. Transformer for single image super-resolution. *2022 IEEE/CVF Conference on Computer Vision and Pattern Recognition Workshops (CVPRW)*, pages 456–465, 2021. 2
- [25] Rafał K. Mantiuk, Scott J. Daly, and Louis Kerofsky. Display adaptive tone mapping. *SIGGRAPH*, 2008. 4
- [26] Rafał K. Mantiuk, Kil Joong Kim, Allan G. Rempel, and Wolfgang Heidrich. Hdr-udp-2: a calibrated visual metric for visibility and quality predictions in all luminance conditions. *SIGGRAPH*, 2011. 3
- [27] Rafał K. Mantiuk, Alexandre Chapiro, Gizem Rufo, Trisha Lian, Rafał K. Mantiuk, Gyorgy Denes, Alexandre Chapiro, and Anton Kaplanyan. Fovvideovdp: A visible difference predictor for wide field-of-view video. *SIGGRAPH*, 40:1–19, 2021. 3, 5
- [28] Rafał K. Mantiuk, Maliha Ashraf, and Alexandre Chapiro. stelacsf: a unified model of contrast sensitivity as the function of spatio-temporal frequency, eccentricity, luminance and area. *ACM Trans. Graph.*, 41(4), 2022. 1
- [29] Rafał K. Mantiuk, Param Hanji, Maliha Ashraf, Yuta Asano, and Alexandre Chapiro. Colorvideovdp: A visual difference predictor for image, video and display distortions. *SIGGRAPH*, 2024. 3, 9
- [30] NVIDIA Corporation. Deep learning super sampling (dlss). <https://www.nvidia.com/en-us/geforce/technologies/dlss/>, 2024. Accessed: 2024-11-15. 1, 2
- [31] NVIDIA Corporation. Nvidia tensor core architecture. <https://www.nvidia.com/en-us/data-center/tensorcore/>, 2024. Accessed: 2024-11-15. 1
- [32] Anjul Patney, Marco Salvi, Joohwan Kim, Anton Kaplanyan, Chris Wyman, Nir Benty, David Luebke, and Aaron Lefohn. Towards foveated rendering for gaze-tracked virtual reality. *ACM Trans. Graph.*, 35(6), 2016. 1, 2
- [33] Robin Rombach, Andreas Blattmann, Dominik Lorenz, Patrick Esser, and Björn Ommer. High-resolution image synthesis with latent diffusion models, 2021. 2
- [34] Christoph Schuhmann, Romain Beaumont, Richard Vencu, Cade Gordon, Ross Wightman, Mehdi Cherti, Theo Coombes, Aarush Katta, Clayton Mullis, Mitchell Wortsman, Patrick Schramowski, Srivatsa Kundurthy, Katherine Crowson, Ludwig Schmidt, Robert Kaczmarczyk, and Jenia Jitsev. Laion-5b: an open large-scale dataset for training next generation image-text models. In *Proceedings of the 36th International Conference on Neural Information Processing Systems*, Red Hook, NY, USA, 2024. Curran Associates Inc. 2
- [35] Robert Shapley, Ehud Kaplan, and Keith P. Purpura. Contrast sensitivity and light adaptation in photoreceptors or in the retinal network. *Contrast Sensitivity (Proceedings of the Retina Research Foundation Symposia)*, 1993. 2
- [36] Alexandros Stergiou and Ronald Poppe. Adapool: Exponential adaptive pooling for information-retaining downsampling, 2022. 8
- [37] Taimoor Tariq, Nathan Matsuda, Eric Penner, Jerry Jia, Douglas Lanman, Ajit Ninan, and Alexandre Chapiro. Perceptually adaptive real-time tone mapping. *SIGGRAPH Asia*, 2023. 3, 5, 6
- [38] O. Tursun, Elena Arabadzhyska-Koleva, Marek Wernikowski, Radosław Mantiuk, Hans-Peter Seidel, Karol Myszkowski, and Piotr Didyk. Luminance-contrast-aware foveated rendering. *SIGGRAPH*, 2019. 3
- [39] Longguang Wang, Yingqian Wang, Xiaoyu Dong, Qingyu Xu, Jungang Yang, Wei An, and Yulan Guo. Unsupervised degradation representation learning for blind super-resolution. *2021 IEEE/CVF Conference on Computer Vision and Pattern Recognition (CVPR)*, pages 10576–10585, 2021. 2
- [40] Xintao Wang, Ke Yu, Shixiang Wu, Jinjin Gu, Yihao Liu, Chao Dong, Chen Change Loy, Yu Qiao, and Xiaoou Tang. Esrgan: Enhanced super-resolution generative adversarial networks. In *ECCV Workshops*, 2018. 2
- [41] Yifan Wang, Federico Perazzi, Brian McWilliams, Alexander Sorkine-Hornung, Olga Sorkine-Hornung, and Christopher Schroers. A fully progressive approach to single-image super-resolution. *2018 IEEE/CVF Conference on Computer Vision and Pattern Recognition Workshops (CVPRW)*, pages 977–97709, 2018. 2
- [42] Andrew B Watson. A formula for human retinal ganglion cell receptive field density as a function of visual field location. *J Vis*, 14(7), 2014. 9
- [43] Bin Xia, Yulun Zhang, Shiyin Wang, Yitong Wang, Xing Wu, Yapeng Tian, Wenming Yang, and Luc Van Gool. Difiir: Efficient diffusion model for image restoration. 2023

- IEEE/CVF International Conference on Computer Vision (ICCV)*, pages 13049–13059, 2023. [2](#)
- [44] Jianchao Yang, John Wright, Thomas Huang, and Yi Ma. Image super-resolution as sparse representation of raw image patches. In *2008 IEEE Conference on Computer Vision and Pattern Recognition*, pages 1–8, 2008. [2](#)
- [45] Wenjun Kevin Zeng, Scott J. Daly, and Shawmin Lei. Point-wise extended visual masking for jpeg-2000 image compression. *International Conference on Image Processing (ICIP)*, 1:657–660 vol.1, 2000. [5](#)
- [46] Roman Zeyde, Michael Elad, and Matan Protter. On single image scale-up using sparse-representations. In *Curves and Surfaces*, pages 711–730, Berlin, Heidelberg, 2012. Springer Berlin Heidelberg. [4](#)
- [47] Richard Zhang, Phillip Isola, Alexei A. Efros, Eli Shechtman, and Oliver Wang. The unreasonable effectiveness of deep features as a perceptual metric. *2018 IEEE/CVF Conference on Computer Vision and Pattern Recognition*, pages 586–595, 2018. [2](#)